THE JOURNAL OF PHYSICAL CHEMISTRY LETTERS
A JOURNAL OF THE AMERICAN CHEMICAL SOCIETY

pubs.acs.org/JPCL

Letter

Energy-Based Interface Detection for Phase Change Processes of Monatomic Fluids in Nanoconfinements

Mustafa Ozsipahi, Yigit Akkus, Chinh Thanh Nguyen, and Ali Beskok*

Cite This: *J. Phys. Chem. Lett.* 2021, 12, 8397–8403

Read Online

ACCESS | Metrics & More | Article Recommendations | Supporting Information

ABSTRACT: An energy-based liquid–vapor interface detection method is presented using molecular dynamics simulations of liquid menisci confined between two parallel plates under equilibrium and evaporation/condensation conditions. This method defines the liquid–vapor interface at the location where the average kinetic energy of atoms first exceeds the average potential energy imposed by all neighboring molecules. This definition naturally adapts to the location of the menisci relative to the walls and can properly model the behavior of the liquid adsorbed layers. Unlike the density cutoff methods frequently used in the literature that suffer from density layering effects, this new method gives smooth and continuous liquid–vapor interfaces in nanoconfinements. Surface tension values calculated from the equilibrium MD simulations match the Young–Laplace equation better when using the radius of curvatures calculated from this method. Overall, this energy-based liquid–vapor interface detection method can be used in studies of nanoscale phase change processes and other relevant applications.

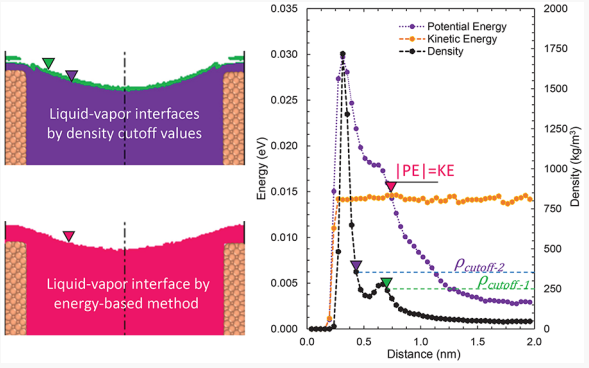

Evaporation in nanocapillaries is at the center of several natural and engineered processes such as transpiration of water in plants,[1] water desalination,[2] and thermal management of photonic and electronic devices.[3] Active mechanisms of evaporation in nanoconfined systems are poorly understood. The dynamics and kinetics of phase transition at the liquid–vapor interfaces at these scales are substantially different from those at the millimeter/micrometer scales because of the increased surface-to-volume ratio that amplifies the interface and wall force-field effects.[4,5] Recent experimental findings exhibit deviations from well-known theoretical expectations such as stretching of the meniscus over the outer surface of the capillary,[6] changes in local evaporation kinetics,[4,7] variations in transport resistance of liquids,[8] evaporation of liquid films spreading outside the capillaries and scale-dependent alterations in the evaporation coefficient.[9]

Point-wise measurements in nanoconfined liquid–vapor interfaces are challenging. Numerical simulations using molecular dynamics (MD) can be used to investigate transport in these three-phase systems. Evaporation from nanocapillaries is a bubble-free process even at temperatures higher than the boiling temperature, and it occurs under steady-state conditions.[8] To mimic these conditions and to obtain reliable statistical averaging, MD simulations should be carried out for steady flows. This can be achieved by numerical tricks such as particle removing and injection at the boundaries[10,11] or by the creation of a continuously pumped steady flow system.[12,13] Regardless of the used approach, determining the exact location of the liquid–vapor interface is challenging.

In the molecular level, the liquid–vapor interface corresponds to a transition region with varying thermophysical properties. The extent of the interfacial region varies based on the thermodynamic state. Even for a liquid–vapor mixture of a pure substance well below the critical temperature (i.e., low vapor pressure systems), the interface is not perfectly flat but corrugated by thermal capillary waves.[14] The corrugated interface can be determined by methods focusing on the identification of the molecules forming it.[15] While early methods using intrinsic sampling or probing[16,17] were able to identify near-flat surfaces, the subsequent works[15,18] generalized these methods for arbitrary interface shapes. Intrinsic geometric/structural analyses basically depend on the atomic positions, which are obtained from the instantaneous configuration of the atoms. However, employment of these can be impractical to determine the interface between two phases containing the same chemical compound, especially in the case of strongly evaporating interfaces.[19] To overcome this issue, a special clustering scheme was proposed for identification of the dividing surface based on a local cutoff density.[20] Employment of a cutoff density to define a

Received: August 2, 2021
Accepted: August 23, 2021
Published: August 26, 2021

https://doi.org/10.1021/acs.jpclett.1c02517
J. Phys. Chem. Lett. 2021, 12, 8397–8403

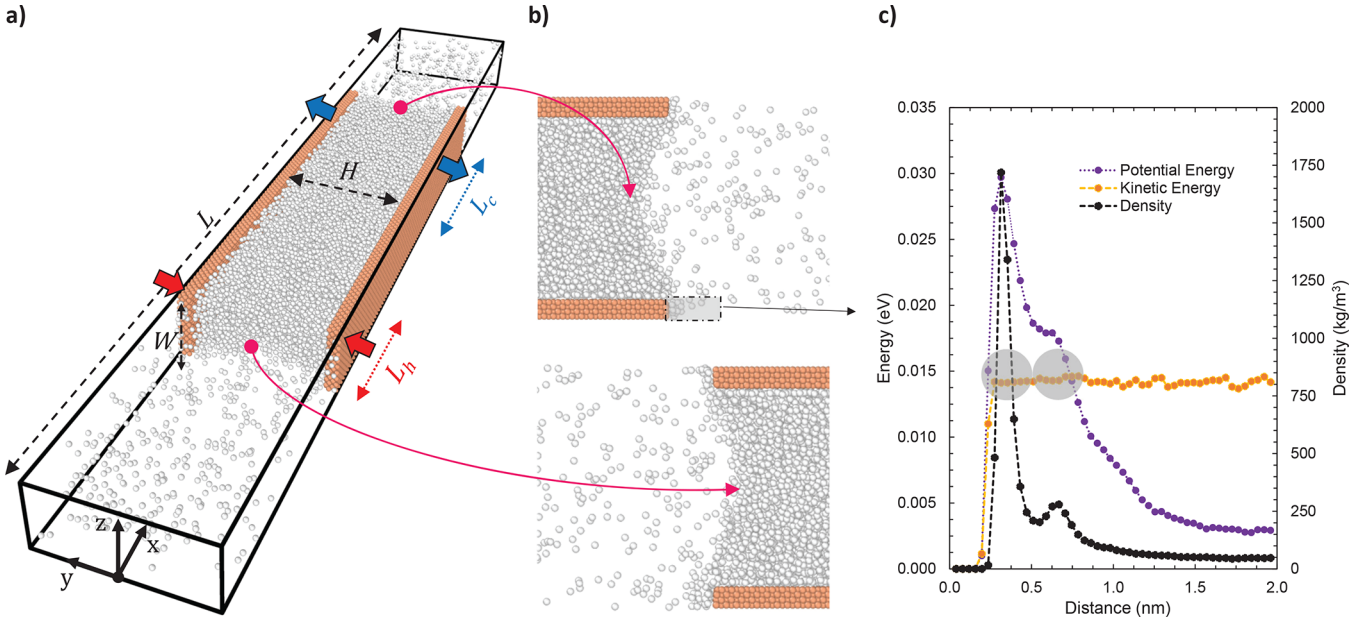

Figure 1. (a) Perspective view of the simulation box of the case M1. Gray spheres represent Ar molecules confined between solid Pt walls (orange spheres). L_h and L_c represent the equal heat extraction/addition regions in the NEMD stage. Wall atoms between the L_h and L_c were frozen in order to eliminate heat conduction between heated/cooled regions of the wall. (b) Instantaneous snapshot of two menisci forming at the end of the *NVE* stage. (c) Energy and density distributions of Ar atoms at the near-wall region, which is shown as a gray box in panel b, calculated using bins with $\Delta x = 0.0392$ nm, $\Delta y = 0.588$ nm, and $\Delta z = 3.92$ nm dimensions. The gray circles in panel c represent atomic diameter of Ar atoms to indicate the scale.

continuous, isodensity interfacial surface was also proposed previously.[21] Consequently, the "cutoff value" of the sufficiently time-averaged fluid density determines the location of the reference surface dividing the phases inside the interfacial region. Different selection criteria have been suggested for the cutoff value; these include the average of the phases' bulk densities,[22] Gibbs's equimolar density,[23] half of the bulk liquid density,[24] arbitrary values between the bulk liquid and vapor densities,[13] and the density value corresponding to the intersection of the extrapolated piece-wise fits applied to the interfacial and bulk vapor region density profiles.[25] The lack of agreement on selection of the cutoff density motivates the current study to seek a new criterion for the detection of interfaces, especially during phase change processes.

Liquids are well-packed, and they evolve through intermolecular interactions. For a given number density, N, the mean molecular spacing for liquids ($\delta = N^{-1/3}$) becomes comparable to the molecular diameter σ. Considering monatomic molecules interacting via van der Waals (vdW) forces modeled by 12−6 Lennard-Jones (LJ) potential, each liquid atom experiences a net attractive (negative) potential energy (PE), because of the contributions from its neighboring molecules. Atoms that are close to the solid boundaries also experience wall attraction, which is modeled here using LJ interactions between the fluid and solid molecules. In addition to their potential energy, the molecules also exhibit thermal motion. The *time-averaged* translational kinetic energy (KE) *per atom in a bin* is given by[26]

$$\mathrm{KE} = \left\langle \frac{1}{2n} \sum_{i=1}^{n} \sum_{a=1}^{3} m_i v_{i,a}^2 \right\rangle = \frac{3}{2} k_B T \tag{1}$$

where n is the number of molecules in a bin and $\langle \cdots \rangle$ shows time averaging. Here, m_i is mass of the ith molecule, and $v_{i,a}$ is the 3 orthogonal components of the velocity of molecule i; k_B is the Boltzmann constant; T is the absolute temperature. Association of the averaged molecular KE with the local temperature is important. Because phase change happens at a constant temperature, each vapor and liquid molecule experiences similar KE, but the PE induced by its neighboring atoms greatly varies with the local density. For example, the PE for vapor molecules is mostly negligible because the mean molecular spacing of vapor molecules is large enough for LJ attraction to be significant.

Comparison of the time-averaged molecular KE and PE at the liquid−vapor interface can help understand the phase change process for (quasi) steady transport. Simply the phase change requires the KE of a molecule to be greater than the *magnitude of the* PE, so that it has enough energy to escape the influence of its surrounding molecules. Considering this, we defined the liquid−vapor interface at a location where the *average molecular* KE *first exceeded the magnitude of the average molecular* PE. Because the energy-well induced by the LJ interactions due to the neighboring molecules lead to attractive (negative) PE, we define the interface at a bin location where KE = |PE|. An energy-based interface definition was *alluded* to in ref 27 for investigation of a vapor film boiling using *transient* nonequilibrium MD simulations. However, their simulations resulted in a moving flat interface, and the authors did not use this interface definition.

In order to test the effectiveness of the proposed method, we investigate equilibrium, evaporation, and condensation dynamics of Ar confined in a nanochannel. The computational setup is similar to the phase change driven nanopump, which was employed in our prior works[12,13] to investigate thin-film evaporation and condensation in nanoconfined domains. It consists of two parallel walls made of platinum (Pt) atoms (orange spheres in Figure 1). In the transverse direction, the domain size is determined by the outermost Pt layers of each

https://doi.org/10.1021/acs.jpclett.1c02517
J. Phys. Chem. Lett. 2021, 12, 8397−8403

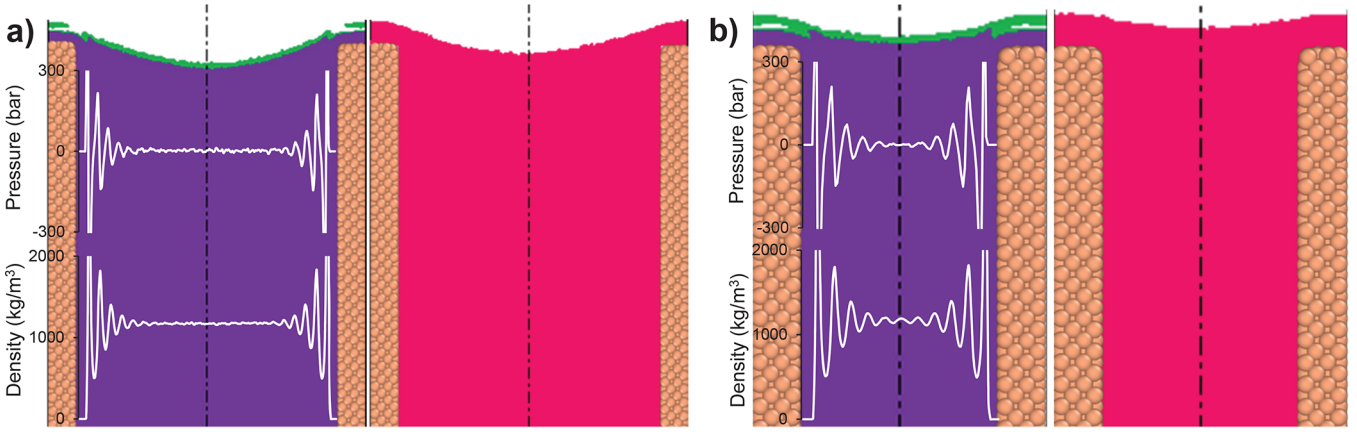

Figure 2. Liquid/vapor interface profiles in (a) M1 and (b) M2 during equilibrium simulations. Left panels show the density-based interfaces, where green and purple represent liquid phases obtained using density cutoff values of 250 and 350 kg/m^3, respectively. Right panels present the energy-based interface, where red shows the liquid phase. Density and pressure distributions inside the midchannel are given as insets in left panels. Reducing the channel height increases the surface forces on Ar atoms, resulting in significant fluctuations for both pressure and density profiles.

wall, while it extends beyond the walls in the longitudinal direction. The fluid atoms (gray spheres in Figure 1) introduced into the system condense in the space between the two walls and form a liquid bridge due to the attraction of Ar atoms with the wall atoms. The rest of the domain is occupied by the vapor phase. Application of periodic boundary conditions connects the opposite ends of the domain enabling a continuous motion of the gas between both liquid−vapor interfaces. By equally heating and cooling the channel atoms at the opposite ends (see Figure 1a), net evaporation and condensation are obtained at the interfaces, respectively. Consequently, a steady liquid flow is established from the condenser to the evaporator through the channel, with a steady gas flow between the two interfaces. Overall, this technique enables the formation of steady evaporating and condensing liquid−vapor interfaces. All molecular dynamics simulations are performed using Large-scale Atomic/Molecular Massively Parallel Simulator (LAMMPS).[28] Computational details are given in the Supporting Information. For all equilibrium MD simulations the thermodynamic state of liquid Argon (Ar) is fixed at T = 110 K and ρ = 1180 kg/m^3 with a quality factor of $x \simeq 0.05$, while all nonequilibrium MD simulations started from this thermodynamic state and ran by equal energy addition and subtraction to/from the wall molecules in the evaporator and condenser sections, respectively.

Three different geometrically scaled computational domains, from the largest to smallest, model 1 (M1), model 2 (M2), and model 3 (M3), are used to investigate size effects on the new interface detection method. The perspective view of the M1 simulation domain is shown in Figure 1a. Snapshots of the atomic positions at the liquid−vapor interface during the equilibrium MD simulations are shown in Figure 1b. The kinetic and potential energy and density distributions of Ar atoms at the side wall of the platinum plate (see the gray box in Figure 1b) are shown in Figure 1c, where x = 0 corresponds to the lattice position of the last wall atom on the edge of the plate. Time-averaged density and energy values are used to determine the interface thickness. The density profile shows two peaks at approximately 0.3 and 0.65 nm from the wall. These two peaks are due to the statistical average of the motion of Ar atoms at respective locations. The first peak is approximately σ_{Ar} (molecular diameter), and the second peak is $2\sigma_{Ar}$ from the wall. Values of the two density peaks are different than that of liquid Ar confined between the two parallel Pt channels shown in the inset of Figure 2a, because this zone shows absorbed layer transitioning to the vapor phase at the edge of the plate. For example, the second density peak is at 270 kg/m^3, which is about 1/4 of the bulk liquid density. Most contributions in the literature, including our previous studies, used an arbitrary density cutoff value to determine the interface. One can choose any cutoff density value between the liquid and vapor Ar densities, and the interface location changes with the chosen density cutoff value. For this specific location, only a density cutoff value smaller than 250 kg/m^3 will include the second density peak. On the other hand, an energy-based interface is defined at the point where the KE (orange line) first surpasses the magnitude of PE (purple line). By this definition, the thickness of the interface at this location is predicted to be slightly larger than two atomic diameters and includes both density peaks from the wall.

Because of the number of evaporating or condensing atoms, the vapor region near the interfaces behaves as a dense gas. The density-based interface detection method is employed using the time-averaged density in each bin, and the interface is identified at the location where the density exceeded its "user decided" cutoff value. Interface predictions under equilibrium MD simulations for M1 and M2 cases using the density cutoff values (250 and 350 kg/m^3) and the energy-based method are shown in Figure 2. Two identical menisci form on the two edges of the parallel plate system, and only one of them is shown in the figures for brevity. The density-based method using the cutoff value of 250 kg/m^3 exhibits discontinuity in the liquid−vapor interface region, because this region has two density peaks, as previously shown in Figure 1c. Furthermore, density layering near the edges of the parallel plate system results in deformation of the meniscus profile around the corner of the walls, and this effect becomes more evident with decreasing the channel height as seen in Figure 2b for the M2 case. Insets in Figure 2 show density and pressure profiles across the liquid section of the channel. The M1 case is large enough to create a constant bulk density and bulk pressure regions, where the M2 case is dominated by the wall force field effects that lead to oscillations. It is important to indicate that pressure in the figures is calculated as the average of the three normal stresses within each bin, and these exhibit anisotropy in the near-wall regions, as previously shown in ref 29. Overall,

https://doi.org/10.1021/acs.jpclett.1c02517
J. Phys. Chem. Lett. 2021, 12, 8397−8403

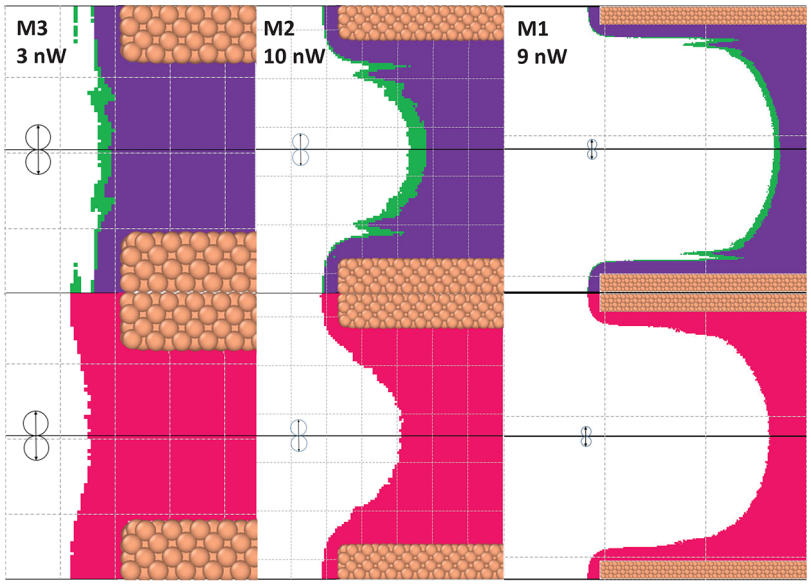

Figure 3. Scale effects on the performance of interface detection methods using energy-based (bottom row) and density-based approaches (top row, where green and purple represent liquid phases obtained using density cutoff values of 250 and 350 kg/m^3, respectively). Various meniscus profiles are obtained using NEMD simulations employing different H/C values. 14950 Ar atoms are used in M1 to have an elongated interface profile. M3 was performed with 1050 Ar atoms. All simulations were performed with ϵ_{Ar-Pt} = 0.00558 eV. A representation of two Ar molecules is shown to indicate the scale.

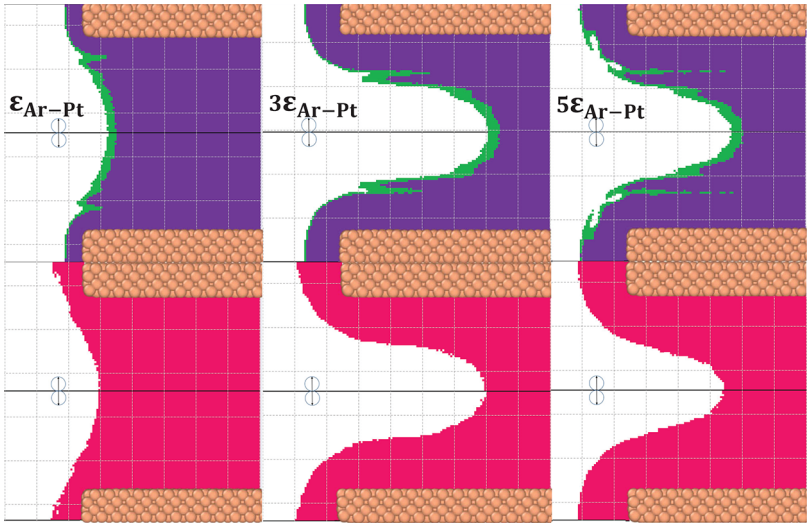

Figure 4. Effect of interface detection methods for different wall−fluid interaction potential strengths. Tests were performed on M2 using 8 nW H/C. Top row: Density-based interface definition. Green and purple colors represent the liquid phases obtained using the density cutoff values of 250 and 350 kg/m^3, respectively. Bottom row: Liquid phase obtained using energy-based interface detection method.

the radius of curvature of the meniscus decreases with increasing the density cutoff value. The energy-based interface detection method results in much smoother liquid−vapor interface regions than the density cutoff method, and it also predicts a larger meniscus radius.

In order to investigate the performance of the energy-based interface detection method under phase change processes, constant heating and cooling are applied in the evaporator and condenser regions of the domain (see Figure 1a). Moreover, the smallest model (M3) is simulated to observe the scale effects. It should be noted that the simulation setup yields steady-state results, and the interface is determined using KE and PE values averaged from 1 000 000 independent samples. The filling ratio of each simulation domain is carefully selected such that the evaporating meniscus is always placed within the heat addition region of the domain, while the condenser section has mostly flat interface (see Figure S1). The menisci in the evaporator regions of the three cases are shown in Figure 3. A pinned meniscus forms under 3 nW heating and cooling (H/C) for the M3 case. The density-based interface detection method is affected by the wall forces and cannot predict a meniscus radius regardless of the density cutoff value. Moreover, adsorbed layer thickness near the wall edges varies significantly with the used cutoff value for the density-based method. These deficiencies are properly addressed in the energy-based method. The M2 case with 10 nW H/C exhibits a receded meniscus, which is located nearly at the center of the heated region (L_h). The energy-based method presents a

https://doi.org/10.1021/acs.jpclett.1c02517
J. Phys. Chem. Lett. 2021, 12, 8397−8403

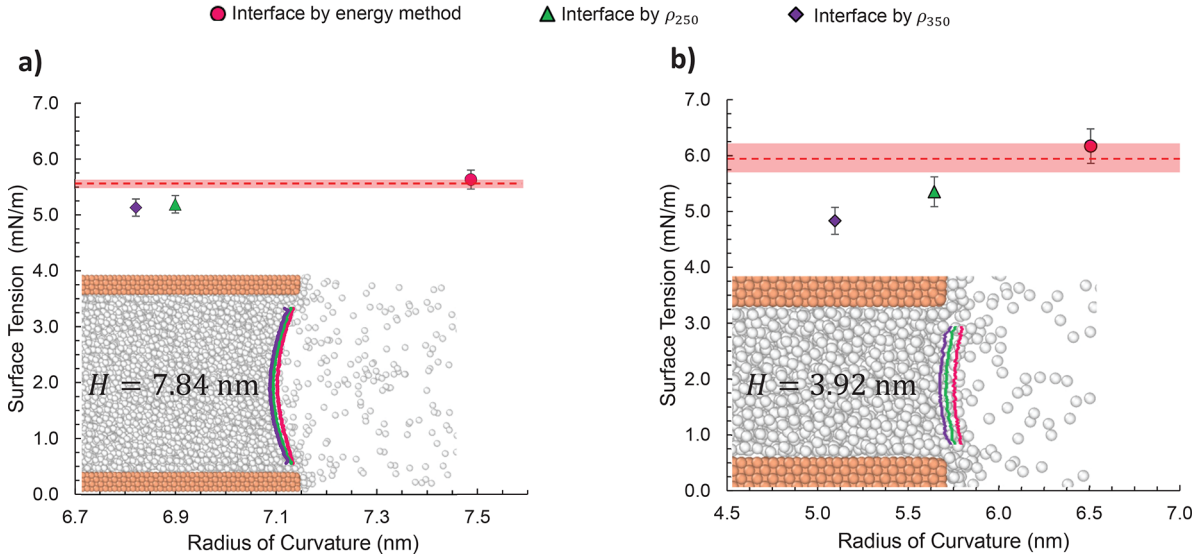

Figure 5. Young−Laplace (data points) and MD (dashed line) calculations of liquid/vapor surface tension for (a) M1 and (b) M2. Insets show the resultant interfaces formed at the channel openings, where the red line represents the interface obtained by the proposed energy-based method, while green and purple lines represent the ones obtained by density cutoff values of 250 and 350 kg/m^3, respectively. Error bars are obtained using various slab thicknesses (group of computational bins) to calculate the pressure difference in the Young−Laplace equation. The red block presents the error bands of liquid/vapor surface tension using 6 different slab heights varying between 0.4 and 1.4 nm.

smooth transition between the meniscus and the adsorbed layer, while the density-based method shows large oscillations for both cutoff values. The M1 case with 9 nW H/C displays an elongated receded meniscus, where the adsorbed layer formation is obvious in and around the channel. The transition region from the intertwined meniscus to the adsorbed layer is smooth for the energy-based method because it eliminates the fluctuations induced by density layering.

Next, we investigate the performance of the new interface detection method under increased wall−fluid interaction potentials. Initial studies were performed using Ar−Pt interactions based on the Lorentz−Berthelot mixing rule, resulting in ϵ_{Ar-Pt} = 0.00558 eV. We systematically increased the wall−fluid interaction potential to three and five times larger than this value while applying 8 nW H/C to the M2 case. The comparison of the interface predictions in the evaporator regions under three different interaction strengths is provided in Figure 4. Upon increasing the wall−fluid interaction potential, PE of the Ar atoms increases, whereas keeping the same heating value between the three cases resulted in similar KE values which is a function of local temperature, as shown in eq 1. Figure S2 shows PE, KE, and density variations obtained in the near-wall region. For increased interaction potentials, evaporation of Ar from the interface is more difficult and this results in thicker adsorbed layers and smaller meniscus radius. Density-based interfaces at two different cutoff values are oscillatory and discontinuous, and they result in different meniscus curvatures.

The scale, wall−fluid interaction potential, and heating/cooling effects are investigated using the density- and energy-based interface detection methods. We show that the energy-based method yields smoother interface profiles with a flatter radius of curvature (ROC). Other physical and thermophysical properties of the interface, such as the area, contact angle, temperature, and pressure, are used in various models and equations, such as the Hertz−Knudsen, Young's, and Young−Laplace equations. In order to compare the predictions of both interface detection methods, we investigate the consistency of the Young−Laplace equation. For this purpose, we use the Young−Laplace equation that relates the pressure drop at the interface with the ROC of the meniscus using surface tension. This requires the calculation of the surface tension and the pressure drop between the liquid and vapor sections of the domain from MD simulation data. It is important to indicate that both quantities require the calculation of normal stresses at each computational bin. Pressure is defined as the average normal stress, which becomes isotropic away from the liquid−vapor interface. Surface tension is calculated as an integral effect of anisotropic normal stress components across the same interface (see section 2 of the Supporting Information for details). Normal stress calculations in MD utilize the Irwing−Kirkwood method, which includes the virial terms that require long-range intermolecular force interactions for accurate calculations.[30] In addition, surface tension in nanoscale can be affected by curvature, capillary wave, and confinement effects.[4,31] The objective of this study is the determination of the advantages of the new energy-based interface detection method, not the exact values of the surface tension or pressure. Accurate calculation of these requires consideration of several factors described in refs 32−36. Here we test the consistency of the Young−Laplace equation when using MD-calculated surface tension and pressure drop, while the ROC is determined using the density cutoff and energy-based methods. Figure 5 presents surface tensions calculated from the Young−Laplace equation using ROCs obtained from different interface detection methods (see the insets for interfacial profiles utilized in ROC estimations) during equilibrium MD simulations. Calculation with the ROC obtained from energy-based method yields surface tension values of γ = 5.63 and 6.17 mN/m for M1 (Figure 5a) and M2 (Figure 5b) cases, respectively, which are in close agreement with the surface tension values calculated from anisotropic normal stresses (dashed lines in Figure 5) during MD simulations. Therefore, for both M1 and M2 cases, the energy-based interface detection method gives consistent ROCs such that the Young−Laplace equation is valid. On

https://doi.org/10.1021/acs.jpclett.1c02517
J. Phys. Chem. Lett. 2021, 12, 8397−8403

the other hand, surface tensions calculated using the ROCs obtained from arbitrarily chosen density cutoff values result in considerable deviations. The extent of deviations increases with decreasing the capillary size.

In summary, a new energy-based interface detection method that identifies the liquid−vapor interface at a location where the average molecular kinetic energy first surpasses the magnitude of the average potential energy is introduced. The performance of this new method is compared with the frequently used density cutoff method using both equilibrium and nonequilibrium MD simulations. Scale, heating and cooling, and wall−fluid interaction potential effects are investigated. The radius of curvatures calculated from both methods is also compared with the predictions from the Young−Laplace equation for consistency. In all presented cases the energy-based interface detection method resulted in smooth and superior results in comparison to the density cutoff method. Our future studies will use this energy-based interface method in the investigation of transport in adsorbed layers, and we also plan to extend the new method for diatomic and more complex molecules. This method can also be applied to droplets, liquid bridges, and multiphase flows and transport in nanochannels.

■ ASSOCIATED CONTENT

Supporting Information

The Supporting Information is available free of charge at https://pubs.acs.org/doi/10.1021/acs.jpclett.1c02517.

Details of the MD simulations and surface tension calculations (PDF)

■ AUTHOR INFORMATION

Corresponding Author

Ali Beskok − *Southern Methodist University, Dallas, Texas 75205, United States;* orcid.org/0000-0002-8838-5683; Email: abeskok@smu.edu

Authors

Mustafa Ozsipahi − *Southern Methodist University, Dallas, Texas 75205, United States;* orcid.org/0000-0003-1378-3991

Yigit Akkus − *ASELSAN Inc., Ankara 06200, Turkey;* orcid.org/0000-0001-8978-3934

Chinh Thanh Nguyen − *Southern Methodist University, Dallas, Texas 75205, United States*

Complete contact information is available at: https://pubs.acs.org/10.1021/acs.jpclett.1c02517

Author Contributions

M.O. performed molecular dynamics simulations. M.O. and Y.A. wrote the manuscript. C.T.N. contributed to the surface-tension calculations. All authors contributed the ideas and discussed the results. A.B. reviewed and edited the manuscript.

Notes

The authors declare no competing financial interest.

■ ACKNOWLEDGMENTS

This material is based upon work supported by the National Science Foundation under Grant No. CBET 2042239. M.O. acknowledges the financial support by the Turkish Scientific and Technological Research Council of Turkey under the project 1059B192000153. Computations were carried out using high-performance computing facilities of the Center for Scientific Computation at Southern Methodist University.

■ REFERENCES

(1) Wheeler, T. D.; Stroock, A. D. The transpiration of water at negative pressures in a synthetic tree. *Nature* **2008**, *455*, 208−212.

(2) Chen, X.; Zhu, Y. B.; Yu, H.; Liu, J. Z.; Easton, C. D.; Wang, Z.; Hu, Y.; Xie, Z.; Wu, H. A.; Zhang, X.; Li, D.; Wang, H. Ultrafast water evaporation through graphene membranes with subnanometer pores for desalination. *J. Membr. Sci.* **2021**, *621*, 118934.

(3) Li, D.; Wu, G. S.; Wang, W.; Wang, Y. D.; Liu, D.; Zhang, D. C.; Chen, Y. F.; Peterson, G. P.; Yang, R. Enhancing flow boiling heat transfer in microchannels for thermal management with monolithically-integrated silicon nanowires. *Nano Lett.* **2012**, *12* (7), 3385−3390.

(4) Li, Y.; Alibakhshi, M. A.; Zhao, Y.; Duan, C. Exploring ultimate water capillary evaporation in nanoscale conduits. *Nano Lett.* **2017**, *17* (8), 4813−4819.

(5) Lee, J.; Laoui, T.; Karnik, R. Nanofluidic transport governed by the liquid/vapour interface. *Nat. Nanotechnol.* **2014**, *9* (4), 317.

(6) Radha, B.; Esfandiar, A.; Wang, F. C.; Rooney, A. P.; Gopinadhan, K.; Keerthi, A.; Mishchenko, A.; Janardanan, A.; Blake, P.; Fumagalli, L.; Lozada-Hidalgo, M.; Garaj, S.; Haigh, S. J.; Grigorieva, I. V.; Wu, H. A.; Geim, A. K. Molecular transport through capillaries made with atomic-scale precision. *Nature* **2016**, *538* (7624), 222.

(7) Lu, Z.; Kinefuchi, I.; Wilke, K. L.; Vaartstra, G.; Wang, E. N. A unified relationship for evaporation kinetics at low Mach numbers. *Nat. Commun.* **2019**, *10* (1), 2368.

(8) Nazari, M.; Masoudi, A.; Jafari, P.; Irajizad, P.; Kashyap, V.; Ghasemi, H. Ultrahigh evaporative heat fluxes in nanoconfined geometries. *Langmuir* **2019**, *35* (1), 78−85.

(9) Li, Y.; Chen, H.; Xiao, S.; Alibakhshi, M. A.; Lo, C. W.; Lu, M.; Duan, C. Ultrafast diameter-dependent water evaporation from nanopores. *ACS Nano* **2019**, *13* (3), 3363−3372.

(10) Røsjorde, A.; Fossmo, D. W.; Bedeaux, D.; Kjelstrup, S.; Hafskjold, B. Nonequilibrium molecular dynamics simulations of steady-state heat and mass transport in condensation: I. Local equilibrium. *J. Colloid Interface Sci.* **2000**, *232* (1), 178−185.

(11) Meland, R.; Frezzotti, A.; Ytrehus, T.; Hafskjold, B. Nonequilibrium molecular-dynamics simulation of net evaporation and net condensation, and evaluation of the gas-kinetic boundary condition at the interphase. *Phys. Fluids* **2004**, *16* (2), 223−243.

(12) Akkus, Y.; Beskok, A. Molecular diffusion replaces capillary pumping in phase-change-driven nanopumps. *Microfluid. Nanofluid.* **2019**, *23* (2), 14.

(13) Akkus, Y.; Koklu, A.; Beskok, A. Atomic scale interfacial transport at an extended evaporating meniscus. *Langmuir* **2019**, *35* (13), 4491−4497.

(14) Ismail, A. E.; Grest, G. S.; Stevens, M. J. Capillary waves at the liquid-vapor interface and the surface tension of water. *J. Chem. Phys.* **2006**, *125* (1), 014702.

(15) Škvor, J.; Škvára, J.; Jirsák, J.; Nezbeda, I. A general method for determining molecular interfaces and layers. *J. Mol. Graphics Modell.* **2017**, *76*, 17−35.

(16) Chacón, E.; Tarazona, P. Intrinsic profiles beyond the capillary wave theory: A Monte Carlo study. *Phys. Rev. Lett.* **2003**, *91* (16), 166103.

(17) Pártay, L. B.; Hantal, G.; Jedlovszky, P.; Vincze, Á.; Horvai, G. A new method for determining the interfacial molecules and characterizing the surface roughness in computer simulations. Application to the liquid−vapor interface of water. *J. Comput. Chem.* **2008**, *29* (6), 945−956.

(18) Sega, M.; Kantorovich, S. S.; Jedlovszky, P.; Jorge, M. The generalized identification of truly interfacial molecules (ITIM) algorithm for nonplanar interfaces. *J. Chem. Phys.* **2013**, *138* (4), 044110.

(19) Sega, M.; Hantal, G.; Fábián, B.; Jedlovszky, P. Pytim: A python package for the interfacial analysis of molecular simulations. *J. Comput. Chem.* **2018**, *39*, 2118.
(20) Sega, M.; Hantal, G. Phase and interface determination in computer simulations of liquid mixtures with high partial miscibility. *Phys. Chem. Chem. Phys.* **2017**, *19* (29), 18968−18974.
(21) Willard, A. P.; Chandler, D. Instantaneous liquid interfaces. *J. Phys. Chem. B* **2010**, *114* (5), 1954−1958.
(22) Santiso, E. E.; Herdes, C.; Müller, E. A. On the calculation of solid-fluid contact angles from molecular dynamics. *Entropy* **2013**, *15* (9), 3734−3745.
(23) Rao, M.; Berne, B. J. On the location of surface of tension in the planar interface between liquid and vapour. *Mol. Phys.* **1979**, *37* (2), 455−461.
(24) Barisik, M.; Beskok, A. Wetting characterisation of silicon (1, 0, 0) surface. *Mol. Simul.* **2013**, *39* (9), 700−709.
(25) Akkus, Y.; Gurer, A. T.; Bellur, K. Drifting mass accommodation coefficients: in situ measurements from a steady state molecular dynamics setup. *Nanoscale Microscale Thermophys. Eng.* **2021**, *25* (1), 25−45.
(26) Frenkel, D.; Smit, B. *Understanding molecular simulation: from algorithms to applications*, volume *1*; Elsevier, 2001.
(27) Cai, S.; Li, Q.; Li, W.; Zhang, L.; Liu, X. Effects of mole fraction and surface wettability on evaporation of Ar/Kr mixtures: A molecular dynamics study. *J. Mol. Liq.* **2020**, *319*, 114189.
(28) Plimpton, S. Fast parallel algorithms for short-range molecular dynamics. *J. Comput. Phys.* **1995**, *117* (1), 1−19.
(29) Barisik, M.; Beskok, A. Equilibrium molecular dynamics studies on nanoscale-confined fluids. *Microfluid. Nanofluid.* **2011**, *11* (3), 269−282.
(30) Irving, J. H.; Kirkwood, J. G. The statistical mechanical theory of transport processes. iv. the equations of hydrodynamics. *J. Chem. Phys.* **1950**, *18* (6), 817−829.
(31) Werth, S.; Lishchuk, S. V.; Horsch, M.; Hasse, H. The influence of the liquid slab thickness on the planar vapor−liquid interfacial tension. *Phys. A* **2013**, *392* (10), 2359−2367.
(32) Mecke, M.; Winkelmann, J.; Fischer, J. Molecular dynamics simulation of the liquid-vapor interface: The Lennard-Jones fluid. *J. Chem. Phys.* **1997**, *107* (21), 9264−9270.
(33) Kwon, S.; Kim, B.; An, S.; Lee, W.; Kwak, W.; Jhe, H. Y. Adhesive force measurement of steady-state water nano-meniscus: Effective surface tension at nanoscale. *Sci. Rep.* **2018**, *8* (1), 8462.
(34) Zaleski, R.; Kierys, A.; Pietrow, M.; Zgardzińska, B.; Błażewicz, A. Influence of different confining matrices on negative pressure in liquid n-heptane investigated using positronium bubbles as a probe. *J. Colloid Interface Sci.* **2020**, *558*, 259−268.
(35) Yang, Q.; Sun, P. Z.; Fumagalli, L.; Stebunov, Y. V.; Haigh, S. J.; Zhou, Z. W.; Grigorieva, I. V.; Wang, F. C.; Geim, A. K. Capillary condensation under atomic-scale confinement. *Nature* **2020**, *588* (7837), 250−253.
(36) Kim, D.; Kim, J.; Hwang, J.; Shin, D.; An, S.; Jhe, W. Direct measurement of curvature-dependent surface tension of an alcohol nanomeniscus. *Nanoscale* **2021**, *13* (14), 6991−6996.

https://doi.org/10.1021/acs.jpclett.1c02517
J. Phys. Chem. Lett. 2021, 12, 8397−8403